Journal of Materials Chemistry C

PAPER

View Article Online
View Journal | View Issue

Cite this: J. Mater. Chem. C, 2019, 7, 3924

Interface engineering of solution-grown silver nanofiber networks designed as flexible transparent electrodes†

Peng Li,‡[a] Xiao Wang,‡[a] Jiangang Ma,*[a] Tingfeng Wang,[bc] Wei Zhang,[a] Haiyang Xu[a] and Yichun Liu[a]

Received 30th November 2018,
Accepted 1st March 2019

DOI: 10.1039/c8tc06047a

rsc.li/materials-c

Metal nanonetworks fabricated by chemical plating of metals on electrospun polymer nanofiber network templates have come into the spotlight for use as flexible transparent electrodes. However, depositing continuous and smooth metal films on hydrophobic polymer nanofiber templates is difficult because of the Volmer–Weber growth of metals. This work reports a simple argon plasma treatment approach to increase the surface energy of the templates and achieve the formation of dense silver layers. Furthermore, instead of using external treatment methods that either require high energy injection or are incompatible with plastic substrates, a low-temperature Joule heat-assisted self-welding method is used to improve the conductivity of the solution-grown Ag nanofibers. Instantaneous Joule heat generated by a direct current can target the high-resistance interfaces formed between the Ag nanoparticles and at the grain boundaries, thus lowering the junction resistance and decreasing the interface scattering. The resulting Ag nanofiber networks exhibit high visible light transmittance of ~91%, low sheet resistance of ~5.4 Ω □$^{-1}$, and good stretchability. These results offer valuable insight into the abilities of plasma treatment and Joule heating to modulate the metal film formation mode on polymer nanofiber surfaces. These interface engineering methods can be extended to the development of polycrystalline metal nanonetwork-based electronics.

Introduction

Flexible transparent electrodes (FTEs) can allow visible light to pass through and collect or inject carriers even during repeated bending operations and are required for use in explosively developing optoelectronic devices such as foldable touchscreen panels, transparent heaters and organic solar cells with wearable forms.[1–6] Although indium tin oxide (ITO) is the most widely used commercial transparent conducting material, it suffers from inherent brittleness and low abundance of raw materials, which hinder its use in flexible electronics.[7] In the past few decades, massive effort has been devoted to developing alternative FTE materials including conducting polymers,[8] carbon nanotubes (CNTs),[9] graphene,[10] metal nanonetworks,[11–14] and hybrids of these materials.[15,16] In particular, metal nanonetworks possess the advantages of easy preparation, high electrical conductivity, and mechanical flexibility. As a result, metal nanonetworks are widely accepted as the most promising candidates to replace ITO in flexible electronics.[17]

Metal nanonetworks are generally prepared by spin or blade coating single-crystal metal nanowires synthesized by a hydrothermal process or by depositing polycrystalline metal films on various mesh templates.[18,19] Although single-crystal metal nanowire networks have the virtue of being compatible with large-area manufacturing processes, they still suffer from a low ratio of length to diameter, poor dispersibility, and high junction resistance.[20] Several effective approaches to lower the junction resistance have recently been developed, including electrochemical Ostwald ripening,[20] and flash light welding.[21] Unfortunately, these methods are usually incompatible with polymer substrates or deteriorate the optoelectronic performance of the metal nanonetworks. In contrast, the metal nanonetworks prepared by metal deposition on various templates, such as electrospun polymer nanofiber (NF) networks,[22–27] cracked resin films,[28–30] and lithography-defined nanopatterns,[31] exhibit good controllability. In particular, electrospinning is a facile low-cost

[a] Key Laboratory for UV-Emitting Materials and Technology, Ministry of Education, Northeast Normal University, 5268 Renmin Street, Changchun 130024, P. R. China. E-mail: majg@nenu.edu.cn
[b] State Key Laboratory of Laser Interaction with Matter, Changchun Institute of Optics, Fine Mechanics and Physics, Chinese Academy of Science, Changchun 130024, P. R. China
[c] University of Chinese Academy of Sciences, Beijing 100049, P. R. China

† Electronic supplementary information (ESI) available. See DOI: 10.1039/c8tc06047a

‡ These authors contributed equally to this work.

method that can produce self-supporting polymer NFs with a diameter of several tens of nanometers to several micrometers and lengths of up to ten centimeters. Using the electrospun NF networks as templates to fabricate various metal NF network FTEs have come into the spotlight. For example, Huang *et al.*[32] reported a highly stretchable Au NF network FTE with a transmittance (T) of ~90% and low sheet resistance (R_s) of ~10 Ω □$^{-1}$. An *et al.*[33] fabricated a CuZr NF network FTE with a T of 90%, low R_s of ~3.8 Ω □$^{-1}$, and high thermal stability. However, these FTEs were fabricated by the conventional metal deposition methods of evaporation and sputtering which often use noble metals inefficiently.

Solution-grown metal NF network FTEs have been attracting increasing attention because of their simplicity, low cost, and scalability.[34–37] Hsu *et al.*[38] synthesized Ag and Cu NF network FTEs *via* electrospinning and electroless deposition. They used an Ag seed layer as the catalytic nucleation site of the polymer NF templates to promote Ag deposition on the templates, along with a hydrophobic surface to suppress Ag deposition on the substrate. Since then, more and more effort has been devoted to the development of solution-grown metal NF network FTEs. For example, Yang and colleagues fabricated a metal NF network FTE with an R_s of 15.6 Ω □$^{-1}$ and T of ~82%, and demonstrated its applicability as the FTE of a polymer solar cell.[3] Testa *et al.* included an electroless sensitizing agent in the electrospinning solution to achieve selectively catalyzed metallization of the electrospun NF template without hydrophobic substrate treatment.[39] Using this process, they obtained a metal NF network with an R_s of 35 Ω □$^{-1}$ and T of ~90%. More recently, our group reported a solution-grown Ag-coated NF elastomer-based resistor-type sensor with an R_s of 9 Ω □$^{-1}$ and T of ~81%.[40]

Although considerable improvements have been made in the quality of solution-grown metal NF network FTEs, their optoelectronic performance still needs to be raised. This is primarily because most metals follow the Volmer–Weber-mode growth and do not effectively form continuous films on the hydrophobic polymer NF surfaces. The chemically plated metals tend to migrate in a disordered manner and coalesce into discrete granules. Increasing the metal layer thickness by lengthening the deposition time usually leads to a drastic decrease in T rather than increases in metal layer continuity and conductivity because of the unavoidable metal deposition on the substrate and continuous growth of metal clusters. However, few studies have focused on modulating the metal-layer formation modes on polymer NFs to improve the performance of solution-processed metal NF network FTEs. Conventional methods to improve the continuity and conductivity of polycrystalline metal films include high-temperature annealing[31] and high-energy light irradiation.[41] However, these methods require high processing power or long treatment time, increase the manufacturing cost, and could damage the underlying substrate or device. Therefore, an approach to form smooth, continuous metal layers on polymer surfaces and that is compatible with plastic substrates is still strongly desired.

The combination of plasma treatment and Joule heating may overcome the shortcomings of the abovementioned methods and provide continuous metal layers on the polymer surfaces. Plasma treatment is a simple and universal strategy for surface modification[42,43] and is expected to be an effective method to improve the wettability of polymer NF surfaces towards metals, because the surface properties of the supporting polymer NFs strongly influence the morphology of the metal coating. Unfortunately, the ability of plasma treatment of polymer NF surfaces to improve solution-processed metal film deposition has not been thoroughly investigated as yet. In addition, current-assisted localized Joule heating is a fast process that can target high-resistance contact points, weld contacting metal granules, and reshape the contact pathway between the metal granules to form a desirable geometry with low resistance to inner and interwire conduction. Although recent reports have demonstrated that Joule heating can weld single-crystal Ag nanowires by controlling the current flow between the two nanowires to lower their contact resistance,[44,45] Joule heating has seldom been used to improve the continuity of the solution-processed metal layers on polymer NFs.

In this study, we develop a simple approach involving argon plasma treatment and a Joule heating-assisted method to improve the optoelectronic performance of solution-processed Ag-coated NF network FTEs. Argon plasma treatment substantially suppresses Ag cluster migration and accelerates Ag lateral growth, providing an efficient route to increase the wettability of the polymer NF surface towards Ag. This leads to Ag-coated NF network FTEs that exhibit increased deposition rate, nanoparticle uniformity, transmittance, and conductivity compared with those of FTEs that did not undergo argon plasma treatment. In the next step, the instantaneous Joule heat generated by a direct-current (DC) voltage can target the high-resistance interfaces between the grain boundaries of Ag granules, thereby reshaping the contact pathway to form a desirable geometry and lower the interface barrier for electron conduction. Using these methods, we fabricate Ag-coated NF network FTEs with a high T of ~91%, low R_s of 5.4 Ω □$^{-1}$, and high mechanical stretching stability that show great potential for use in wearable electronics.

Results and discussion

Fig. 1 illustrates the synthesis procedure of the Ag-coated NF network FTEs, which involved three main steps. First, a polyvinyl butyral (PVB)/tin chloride ($SnCl_2$) NF network was electrospun on a metal frame from a mixed solution of PVB and $SnCl_2$ as an electrospun precursor and then treated by argon plasma. The argon plasma-treated PVB/$SnCl_2$ NF network was transferred onto a polydimethylsiloxane substrate that was pre-coated with a hydrophobic PVB film to make it more energetically unfavorable for metal nucleation. Second, the sample was immersed in $AgNO_3$ solution. During this step, Ag^+ was reduced by Sn^{2+} and a uniform Ag nanoparticle seed layer formed on the PVB NF surface. The Ag nanoparticles could act as catalyst and nucleation sites for the

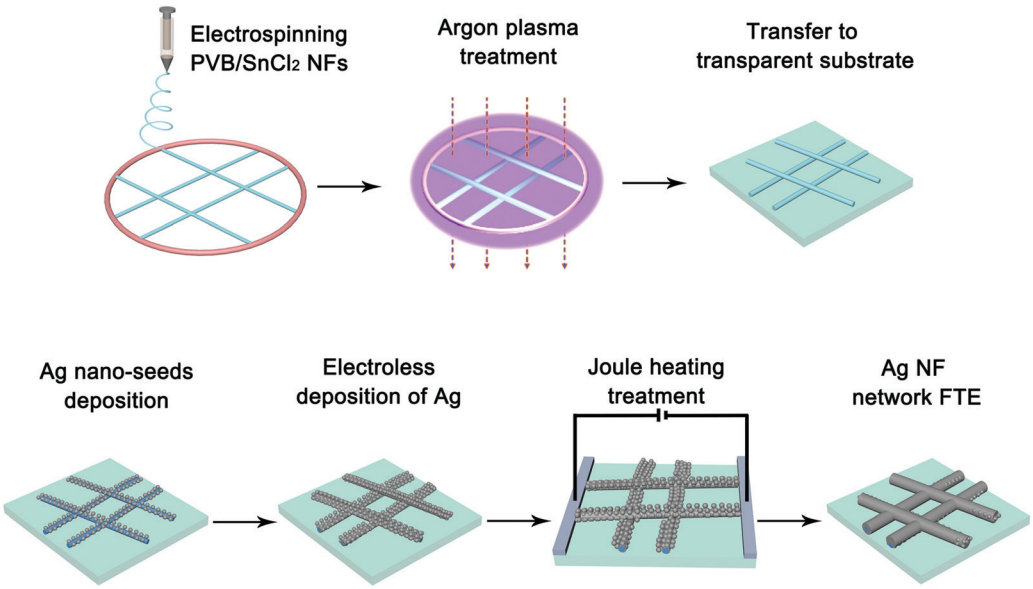

Fig. 1 Overview of the preparation process of the Ag-coated NF network FTEs.

subsequent Ag deposition. The Ag-coated NF network was obtained by electroless deposition of Ag onto the Ag-seeded PVB NF network. Finally, Ag-paste electrodes were coated on the two ends of the Ag-coated NF network, and a constant DC was applied to the Ag-coated NF network to complete the ripening of the FTEs.

The morphology of Ag nanoparticle seed layers on the PVB NFs was examined using transmission electron microscopy (TEM). Fig. 2a and b depict TEM images of the Ag nanoparticle seed layers deposited on the PVB NFs without and with argon plasma treatment, respectively. The surface morphology of the PVB NFs remained almost unchanged after the argon plasma treatment. The average diameter of the PVB NFs was about 150 nm. A high-resolution TEM image of an Ag nanoparticle showed that its lattice spacing was 0.23 nm, which corresponds to the (111) plane of Ag. The corresponding selected-area electron diffraction ring pattern confirmed the formation of Ag (Fig. S1a–c, ESI†). The Ag nanoparticles formed on the argon plasma-treated PVB NFs were smaller and more uniformly dispersed than those formed on the untreated PVB NF surface. This observation was confirmed by the uniform color distributions in the energy-dispersive spectral mapping of Sn and Ag for the plasma-treated PVB NF surface (Fig. S1d–f, ESI†).

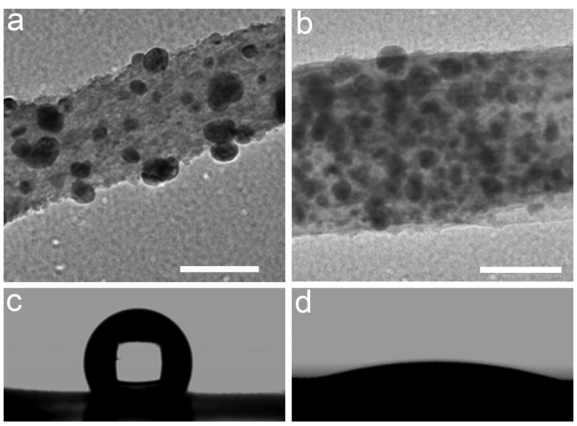

Fig. 2 TEM images of the Ag nanoparticle seed layers grown on (a) untreated and (b) argon plasma-treated PVB NFs. Scale bars are 50 nm. Contact angles of water droplets on (c) untreated and (d) argon plasma-treated PVB NF networks, respectively.

To clarify the exact role of argon plasma treatment in altering the nucleation mode of Ag on the PVB NF surfaces, a surface energy analysis was performed because the physical and chemical properties of the PVB NF surface are thought to greatly affect the surface diffusion behavior of noble metals. As shown in Fig. 2c and d, the argon plasma treatment decreased the contact angle of a deionized water droplet on the PVB NF network from 119° to 29°. According to the Johnson–Kendall–Roberts theory, the surface energy is inversely proportional to the contact angle,[46] implying that the argon plasma treatment increases the surface energy of the PVB NFs. These observations are consistent with previous results and indicate that the plasma treatment generated polar oxygen-containing functional groups on the PVB NF surface.[47] These highly reactive functional groups can interact with Ag atoms to form coordination bonds, which anchor the Ag atoms to the NF surface. Therefore, the wettability of the PVB NF surface for Ag was increased by inhibiting the escape and diffusion of unstable nuclei on the argon plasma-treated PVB NF surface.

The influence of the argon plasma treatment on the growth mode of Ag was investigated by evaluating the change of morphology of the Ag-coated NFs with the electroless deposition time. For comparison, the morphology of Ag-coated NFs that were prepared using untreated PVB NFs was also characterized by scanning electron microscopy (SEM). Fig. 3 presents SEM images of Ag-coated NFs prepared by using the untreated and argon plasma-treated PVB NFs as templates and electroless

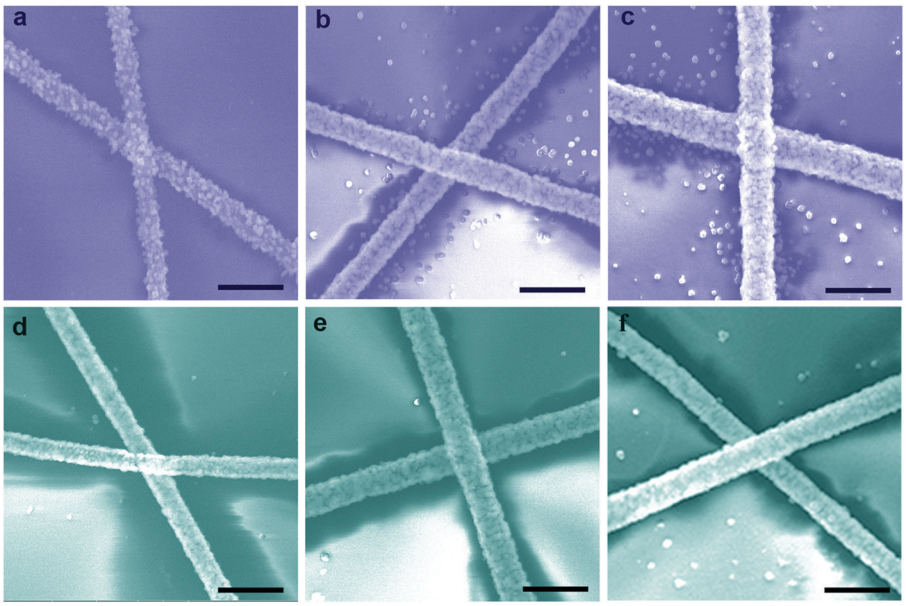

Fig. 3 SEM images of the Ag-coated NFs prepared from (a–c) untreated and (d–f) argon plasma-treated PVB NFs. NFs were prepared with electroless deposition times of (a and d) 10 min, (b and e) 20 min, and (c and f) 30 min. Scale bars are 1 μm.

deposition times of 10, 20, and 30 min. The Ag-coated NFs prepared on the argon plasma-treated PVB NFs for 10 min exhibited a smooth and continuous morphology (Fig. 3d). In contrast, the Ag granules formed after 10 min on the PVB NFs without argon plasma treatment were discrete and rough (Fig. 3a). These differences in the evolution of the Ag clusters are ascribed to the different surface energies of the treated and untreated PVB NF templates. Although the preformed Ag nanoparticle seeds on the PVB NFs can lower the nucleation barrier of Ag, the water-insoluble PVB NFs had low surface energy and poor Ag wettability; thus, the Ag nanoparticle seeds that formed on the untreated PVB NFs were non-uniform and the chemically plated Ag nanocrystals tended to nucleate around the Ag nanoparticle seeds. As a result, the Ag granules deposited on the untreated PVB NFs were rough and discrete. In contrast, the argon plasma treatment markedly improved the wettability of the PVB NF surfaces for Ag, which facilitated Ag deposition. Additionally, the preformed Ag nanoparticles were uniformly dispersed on the plasma-treated PVB NF surfaces, which further promoted the formation of a smooth Ag layer during the subsequent electroless deposition process.

As the deposition time was extended, the adjacent Ag granules coalesced into thick three-dimensional clusters on the untreated PVB NF surface, leaving many unfilled voids at the grain boundaries (Fig. 3b). In addition, several small Ag nanoparticles appeared on the substrate. These nanoparticles were attributed to Ag nucleation on the substrate in the initial electroless deposition stage. Because only a small amount of disperse Ag nanoparticle seeds were preformed on the untreated PVB NFs, the Ag nucleation barrier on the PVB-coated substrate was not much higher than that on the Ag-seeded PVB NFs; thus, Ag nucleation occurred on the substrate. With lengthening electroless deposition time, the Ag nanoparticles on the nucleation sites became larger. In contrast, the bridged and connected clusters became the dominant morphological features of the Ag layer on the treated PVB NF surface; few Ag nanoparticles were deposited on the substrate after 20 min (Fig. 3e, see Fig. S2 (ESI†) for large-area optical and SEM images of the PVB/$SnCl_2$ NFs and Ag-coated NFs). We attributed this phenomenon to the large surface energy difference between the argon plasma-treated PVB NFs and PVB-coated substrate surfaces. These results agree well with the contact angles of water droplets on the treated and untreated PVB surfaces mentioned above. Further extending the electroless deposition time to 30 min resulted in a continuous Ag layer on the untreated PVB NFs (Fig. 3c), but numerous Ag nanoparticles were deposited on the substrate. The Ag-coated NFs prepared with treated PVB NFs as templates and an electroless deposition time of 30 min (Fig. 3f) had a larger diameter and cleaner substrate than those of the NFs prepared with untreated PVB NFs (Fig. 3c).

The deposition time is the main parameter that determines the optoelectronic performance of the Ag-coated NF network FTEs, and thus the dependence of Ag thickness, R_s, and T on the deposition time was investigated. The thickness of the Ag film on the PVB NFs was obtained by statistical analysis of TEM and SEM images, and was considered half of the mean value of the difference between the diameter of PVB NFs and diameter of Ag-coated NFs at a certain deposition time. Fig. 4a shows the time dependence of the thickness of Ag-coated NFs. The red and black curves represent the Ag film thicknesses on the treated and untreated PVB NFs, respectively. The slopes of these curves represent the Ag growth rate. The Ag growth rate on the treated PVB NF templates was much higher than that on the untreated templates in the initial 20 min of deposition. This phenomenon was ascribed to the difference in wettability between the treated and untreated PVB NFs. As the electroless

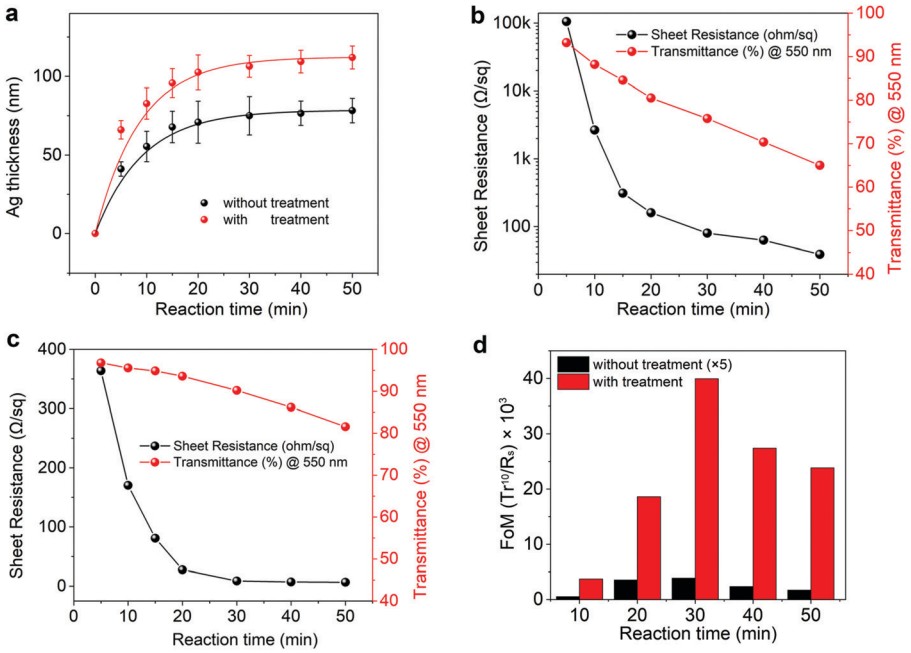

Fig. 4 (a) Dependence of Ag thickness on the electroless deposition time of the treated and untreated PVB NF templates. Dependence of sheet resistance (R_s) and transmittance (T) at 550 nm on the electroless deposition time of the Ag-coated NF network FTEs prepared using (b) untreated and (c) treated PVB NF templates. (d) Dependence of the figure of merit (FoM = T^{10}/R_s) on the electroless deposition time of the Ag-coated NF network FTEs prepared using untreated and argon plasma-treated PVB NF templates.

deposition time extended, the Ag growth rate slowed and the Ag thickness hardly increased after a deposition period of 40 min because of the continuous decrease in glucose concentration. The growth rate achieved here was much faster than that obtained previously, for in which an incubation period of about 25 min was required.[38] According to the mixed potential theory,[48] the reducing agent and metal ions need to reach the same potential before deposition occurs, and the incubation time strongly depends on the electroless deposition conditions, such as the catalyst, reactant ratio, and stirring temperature.[49] In this work, the volume of glucose solution and dripping rate of Tollens' reagent were carefully optimized to shorten the incubation time and effectively facilitate glucose oxidation to reach the same potential as that of Tollens' reagent. Thus, the steady-state electroless deposition occurred after a brief incubation period of less than one minute.

Fig. 4b and c show the dependence of R_s and T (at 550 nm) on the electroless deposition time of the Ag-coated NF network FTEs prepared with untreated and argon plasma-treated PVB NF network templates. Both R_s and T of all FTEs decreased with lengthening deposition time. In the first 10 min, R_s of the FTEs prepared with treated templates decreased faster than that of the FTEs prepared with untreated templates. These results were consistent with the thickness changes of Ag-coated NFs with deposition time. Additionally, T of the FTEs prepared with treated templates decreased slowly because of the increasing diameter of the Ag-coated NFs. In contrast, T of the FTEs prepared with untreated templates decreased quickly because of the rough surface of the Ag-coated NFs and the scattering and plasma resonance absorption of the discrete Ag granules. As the reaction time lengthened to 30 min, R_s of the FTEs fabricated using the plasma-treated templates became very low, although the decrease rate slowed down, and T decreased by 5%. For the FTEs prepared with untreated templates, R_s was still high and T had already decreased by 20%. These results agree well with the morphology evolution of the Ag-coated NFs observed in the SEM images. The high R_s and low T of the untreated Ag-coated NF network FTEs could be ascribed to the poor Ag layer continuity on the PVB NF templates and the Ag nanoparticles deposited on the substrate. The large-area SEM images of the Ag-coated NF network FTEs prepared with untreated and treated templates in Fig. S3 (ESI†) further confirmed this reasoning.

To achieve a high optoelectronic performance, the Ag-coated NF network FTEs need to exhibit high T and low R_s simultaneously. The widely used figure of merit (FoM) for transparent conducting materials defined as FoM = T^{10}/R_s was employed to evaluate the performance of the Ag-coated NF network FTEs.[50,51] Based on the data in Fig. 4b and c, the deposition time-dependent FoMs of the FTEs were calculated; the results are presented in Fig. 4d. The FTEs prepared with treated PVB NF networks as templates exhibited much higher FoMs than those of the FTEs prepared with untreated templates. The FTEs showed the highest FoM when the electroless deposition time was 30 min, which suggests a trade-off relationship between T and R_s. Thus, 30 min was used as the deposition time in this work unless otherwise noted. Additionally, T and R_s of the FTEs can be controlled by varying the electrospinning time (Fig. S4, ESI†).

We demonstrated that the template wettability for Ag was enhanced by inhibiting the diffusion of unstable nuclei on the

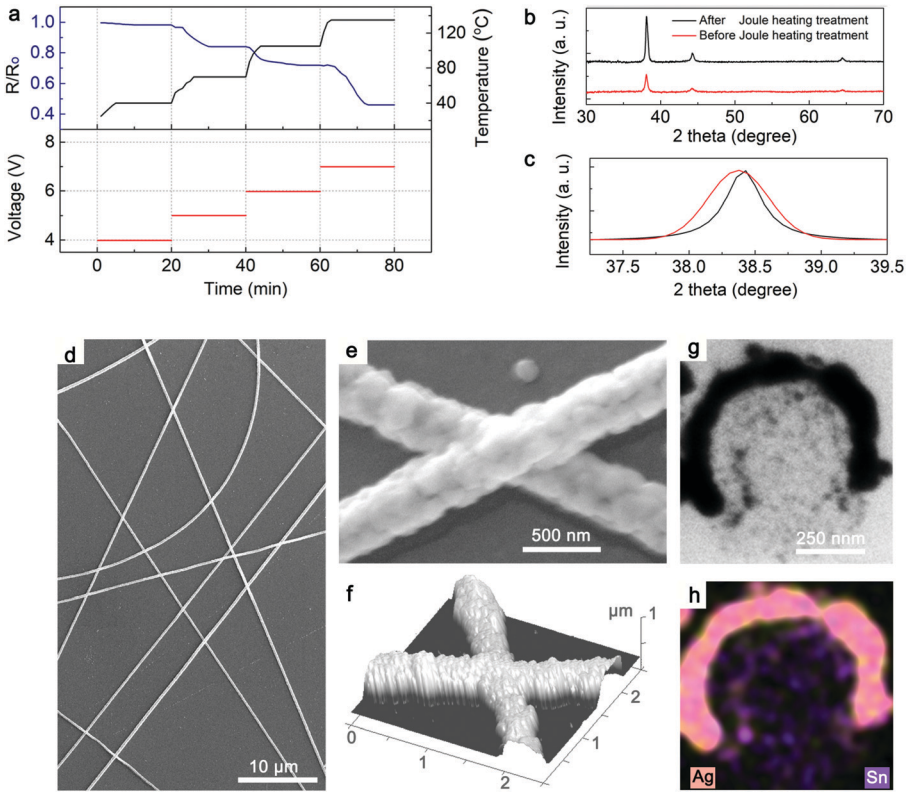

Fig. 5 (a) Changes of resistance and temperature of the Ag-coated NF network FTEs with applied DC voltage and time. (b) The XRD pattern of the Ag-coated NF network FTEs before and after Joule heating treatment. (c) Magnified view of the Ag(111) reflection peak of the Ag-coated NF network FTEs before and after the Joule heating treatment. (d) Large-area and (e) high-magnification SEM images of an Ag-coated NF network FTE after Joule heating treatment. (f) Three-dimensional AFM image showing that the height of the junction between the adjacent Ag-coated NFs was similar to that of an individual Ag-coated NF. (g) A cross-sectional TEM image of the Ag-coated NF after Joule heating treatment and (h) its corresponding element mapping image showing the distributions of Ag and Sn.

supporting polymer NF template surfaces, thereby aiding the formation of continuous and smooth Ag-coated NFs in a short electroless deposition time. To further improve the conductivity of the Ag-coated NF network FTEs, elaborate Joule heating experiments were designed and conducted because the contact interfaces of the deposited Ag nanoparticles are thought to greatly affect the conduction behavior of Ag-coated NFs. Current flowing through a resistor immediately generates Joule heat, which can raise the temperature of the resistor. The temperature increase of a resistor can be controlled by regulating the input voltage or current. For the Ag-coated NF network FTEs prepared on a substrate, the Joule heat-induced temperature increase of the Ag-coated NF network is much higher than that of the supporting substrate.[52]

Fig. 5a shows the relative resistance (R/R_0, where R represents the room-temperature resistance of the Ag-coated NF network FTE after the Joule heating treatment, and R_0 is the original resistance of the Ag-coated NF network FTE) and surface temperature change over time of the Ag-coated NF network FTEs under different applied DC voltages. At a low applied voltage of 4 V, R/R_0 of the Ag-coated NF network FTE was almost unchanged over 20 min. When 5 V was applied to the Ag-coated NF network FTE, R/R_0 decreased to 0.82 during the first 10 min and then remained stable even though the constant voltage was applied for another 10 min. As the input voltage increased, R/R_0 decreased further and then became stable again after several minutes. The R/R_0 of the Ag-coated NF network FTEs strongly depended on the input voltage. Increasing the input voltage to 7 V decreased R/R_0 of the Ag-coated NF network FTE to 0.45, and the maximum temperature of the supporting substrate remained lower than 129 °C. However, we found that when the applied voltage increased to 8 V, R/R_0 of the Ag-coated NF network FTEs no longer decreased even though the average substrate surface temperature reached 151 °C. At an applied voltage of 10 V, the substrate surface temperature increased to 200 °C, and then dropped suddenly. This was because the Ag-coated NFs melted as a result of the high temperature reached because of the large amount of Joule heat produced (Fig. S5, ESI†).

The exact role of Joule heating treatment in altering the conductivity of Ag on the polymer NF template surfaces is unclear. Therefore, SEM, X-ray diffraction (XRD), atomic force microscopy (AFM), and high-angle annular dark field scanning transmission electron microscopy (HAADF-STEM) analyses were performed to elucidate the structural evolution responsible for the abrupt conductivity transition of the Ag layers. The XRD patterns of the untreated Ag-coated NFs and those treated by Joule heating are shown in Fig. 5b. The average Ag grain sizes for

the Ag-coated NFs before and after Joule heating treatment, which were estimated from the XRD peak widths using the Scherrer equation, were ~18 and ~58 nm (Fig. 5c), respectively. Clearly, the Joule heating leads to larger Ag grains and thus a lower density of grain boundaries. The electrical conductivity of metal films that have a thickness higher than the mean free path of electrons suffers from grain boundary scattering, which strongly suppresses the electron mobility. Thus, the larger grain size of the Ag-coated NFs after Joule heating treatment could decrease the number of grain boundaries and suppress electron scattering.

The morphology of the Ag-coated NFs after Joule heating treatment was examined by SEM and AFM. The SEM images of the Joule heating-treated Ag-coated NFs are shown in Fig. 5d. The low coverage rate of the Ag-coated NFs ensured the high T of the FTEs. The low R_s of the Ag-coated NF network FTEs can be attributed to the continuity of Ag NFs in both the micro and the macro scale, the improved conductivity of each NF and the reduced junction resistance of overlapped NFs after the Joule heating treatment. A high-magnification SEM image is shown in Fig. 5e. The Ag-coated NFs exhibited smooth surfaces, suggesting that self-welding occurs at the contact interfaces between the adjacent Ag nanoparticles. Additionally, a three-dimensional AFM image (Fig. 5f) reveals that the height of the junction point between NFs was much lower than the thickness sum of two Ag-coated NFs, indicating that the Ag-coated NFs were fused together. A STEM image and the element mapping of an individual Joule heating-treated Ag-coated NF confirmed the continuity of the Ag layer. As shown in Fig. 5h, the Ag layer was coated on the top half of the PVB NF surface. It is noteworthy that a small breach was observed in the Ag layer, which is obvious in the element mapping image (Fig. 5g). These results demonstrate that the Joule heating treatment enabled the gradual growth of individual nanocrystals until they merged with neighboring nanocrystals to form a continuous flat film. Therefore, the Ag-coated NF FTE treated by Joule heating exhibited a higher conductivity than that of the untreated FTE, which had a discontinuous granular morphology that may have caused substantial interface scattering.

Based on the above results, we propose an explanation for the morphology evolution during the Joule heating treatment of the Ag layers formed on the PVB NF surface. Before the Joule heating treatment, the Ag layers on the PVB NFs consisted of stacked nanoparticles. Early during the Joule heating treatment, the current density was not homogeneous across the Ag-coated NFs because of the high contact resistance between the adjacent Ag-coated NFs or the Ag nanoparticles in a single Ag-coated NF. Therefore, current crowding would occur at these contact interfaces as the electrons travel through them. A previous simulation established that this current crowding can increase the local current density by an order of magnitude.[53] The region with high current density induced by the current crowding could behave like a hot spot in the Ag-coated NF network FTEs. It is widely accepted in copper interconnect technology that surface diffusion-induced electromigration can occur at a current density of 10^6 A cm^{-2} once the silica device operation temperature reaches 100 °C.[54] Additionally, according to Gibbs–Thomson theory, the Gibbs free energy of a nanoparticle is inversely proportional to its radius. The Ag-coated NFs with a stacked nanoparticle structure suffer from high Gibbs free energy and are therefore comparatively unstable. Previous studies have established that the surface diffusion of Ag is possible at room temperature because of its low activation energy of ~1 eV.[55] The average current density of the Ag-coated NF network was about 10^6 A cm^{-2}, suggesting that the current density at the contact interfaces was around 10^7 A cm^{-2}. The localized temperature increase produced by strong Joule heating could provide the Ag atoms with enough thermal energy to diffuse rapidly to lower the surface energy. The regions with high current density at the contact interfaces promoted electromigration and facilitated continued atomic movement *via* sustained Joule heating. The Joule heating-promoted surface and bulk diffusion behavior of the Ag induced welding of the adjacent Ag nanoparticles to achieve a larger contact area. Eventually, an effective contact formed. This was a self-limiting process because the local Joule heat would decrease once the contact resistance was lowered.

Fig. 6a compares the R_s and T (at 550 nm) of the Ag-coated NF network FTEs with those of landmark transparent conducting materials reported in the literature. The Ag-coated NF network FTEs prepared in this study showed low R_s (5.4 Ω □$^{-1}$) and high visible light transmittance (91%). The optoelectronic performance of the Ag-coated NF network FTEs was superior to those of transparent conducting materials composed of CNTs,[9] graphene,[10] Ag nanowires,[45,56,57] and commercial ITO film.

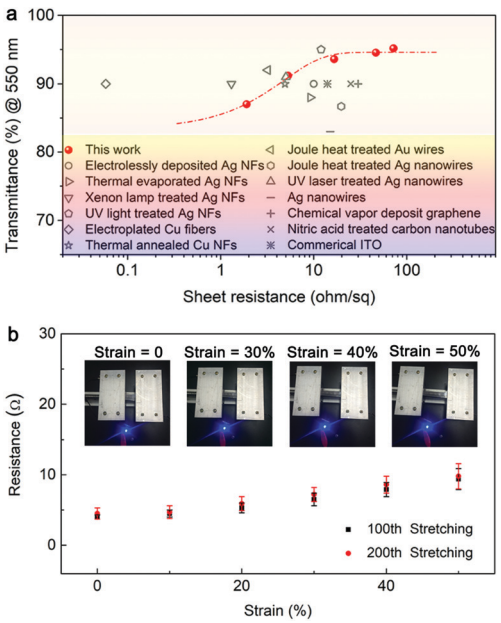

Fig. 6 (a) Plot of sheet resistance *versus* optical transmittance at 550 nm of the Ag-coated NF network. For comparison, the optoelectronic performances of some reported landmark transparent conductors are also given. (b) Resistance changes of the Ag-coated NF network FTEs with stretching strain in the 100th and 200th stretching cycles. The insets are photographs of the Ag-coated NF network FTE in an LED circuit at various tensile strains.

The optoelectronic performance of the Ag-coated NF network FTEs was better than that of thermally evaporated Ag nanotrough networks fabricated using polymer NF networks as templates.[14] Additionally, for materials with a T above 90%, R_s of the Ag-coated NF network FTEs is lower than that of previously reported solution-processed Ag-coated NF networks[38] and comparable with those of Cu NF networks[37] and Au wire networks[44] fabricated at high temperature.

The thickness of the metal layer strongly influences the R_s of metal nanonetworks. For instance, the electroplated Cu fibers with micrometer-scale Cu thickness exhibited R_s lower than 0.1 $\Omega\ \square^{-1}$ and a high T exceeding 90%.[58] The treatment methods developed in this work enable the Ag-coated NF network FTEs to possess comparable optoelectronic performance to that of UV-irradiated Ag-coated NF networks with an Ag thickness twice that of our Ag-coated NFs.[41,59] The features of low R_s and high T achieved simultaneously here demonstrate that interface engineering can effectively improve the optoelectronic performance of solution-grown polycrystalline metal nanonetworks. The resulting Ag-coated NF network FTEs are suitable for use in high-standard optoelectronic devices such as solar cells, light-emitting diodes (LEDs), and transparent heaters.

In addition to the optoelectronic properties, mechanical compliance is important to realize flexible electronics. The flexibility of the Ag-coated NF network FTEs was investigated by measuring their resistance change as a function of stretching strain. As shown in Fig. 6b, the real-time resistance of the Ag-coated NF network FTE (initial resistance 4.1 Ω) was raised slightly when the stretching strain was increased to 50%. However, the resistance returned to its original value once the strain was released. The resistance change under applied strain was measured again after 200 stretch/release cycles. It was found that the resistance change was similar to that of the 100th cycle. To further demonstrate its flexibility, the Ag-coated NF network FTE was used in an LED circuit at various strains. The luminance of the LED did not decrease when the strain was increased from 30% to 50% because of the low resistance increase of the Ag-coated NF network FTE. Fig. S6 (ESI†) shows that the Ag-coated NFs remained continuous even after 200 stretch/release cycles. The stretchability of the FTEs was attributed to the slippage and rearrangement of the Ag-coated NF networks.[40] The real-time resistance of the Ag-coated NF network FTEs responding to repeated bending actions was measured by fixing the FTE on a finger joint (Fig. S7, ESI†). We found that the resistance of the FTE was nearly 5 Ω when the finger was flat, and it increased immediately if the finger bent. Once the finger reverted, the resistance was back to 5 Ω again. These results demonstrated that the Ag-coated NF network FTEs have application potential in wearable sensors, and the performance enhancement methods developed in this work are compatible with polymer substrates.

Conclusion

In summary, we developed an effective method to enhance the performance of solution-grown Ag-coated NF network FTEs *via* the combination of argon plasma treatment and Joule heat-assisted self-welding processes. The argon plasma-treated PVB NF templates had higher surface energy and better Ag wettability than those of the untreated templates. As a result, the Ag layers on the treated templates exhibited more uniform Ag nanoparticle seed distribution, faster growth rate, and smoother Ag film morphology than those of the Ag layers on the untreated templates. Additionally, the electrical conductivity of the Ag-coated NF network FTEs was improved by optimizing the input DC voltage. It was found that the localized Joule heating targeted the high-resistance interfaces between the Ag granules and at the grain boundaries in the Ag-coated NFs, and thus helped to reshape the contact pathways and lower the interface barrier for electron conduction. Using these methods, we were able to fabricate Ag-coated NF network FTEs with a high transmittance of ~91%, low sheet resistance of 5.4 $\Omega\ \square^{-1}$, and stability towards mechanical stretching. Interface engineering can be used to improve the conductivity of other polycrystalline metal networks designed for use in flexible electronics.

Experimental section

Electrospinning and Ag nano-seed deposition

The solution for electrospinning consisted of 8 wt% of polyvinyl butyral (PVB, Aladdin) and 10 wt% of anhydrous tin(II) chloride (Sinopharm) in *n*-butanol (Aladdin) by stirring at 600 rpm with a magnetic stirrer for 4 h. Electrospinning was completed using a homemade setup. The electrospun precursor solution was loaded in 5 mL syringes with a needle tip. The collector was a metal frame. The electrospinning conditions were as follows: a distance of 20 cm between the tip and collector, an applied voltage of +8 kV, and a solution flow rate of 1 mL h^{-1}. Argon plasma treatment of PVB/$SnCl_2$ NFs was performed at a power of 30 W and a plasma treatment time of 5 min. The argon plasma-treated PVB/$SnCl_2$ NFs were transferred onto different transparent substrates (Glass slide or PET). Then, the argon plasma-treated PVB/$SnCl_2$ NFs were immersed into 25 g L^{-1} of $AgNO_3$ (99.9995%, Sinopharm) aqueous solution to grow Ag catalytic nano-seed layers for 30 min. Then the samples were repeatedly washed with deionized water.

Ag electroless deposition

Electroless deposition was achieved by using Tollen's reaction. The sample was immersed vertically into a uniformly stirred 5 g L^{-1} of glucose (anhydrous, Sinopharm) aqueous solution, which worked as a reducing agent. The $Ag(NH_3)^{2+}$ solution was prepared by adding ammonium hydroxide (NH_4OH, 28–32%) into 5 g L^{-1} $Ag(NO)_3$ aqueous solution dropwise until the solution became clear. The $Ag(NH_3)^{2+}$ solution was injected into a 50 mL syringe using a plastic tube. We used a propeller to propel the $Ag(NH_3)^{2+}$ solution dropwise into the reducing agent at a rate of 1 mL min^{-1}. The thickness of the Ag NFs was controlled by adjusting the electroless deposition time.

Characterization

The contact angles of the PVB NF surface were measured using a drop shape analyzer system (Kruss, DSA100). The Ag seed

layer was observed using transmission electron microscopy (TEM, JEOL-2100). The cross-section morphologies of the Ag NFs were examined using a Tecnai G2 F20 S-Twin. The Ag NFs were characterized by scanning electron microscopy (SEM, Hitachi S-4800) and atomic force microscopy (AFM, Bruker) in the scanAsyst mode. The compositions of the Ag NFs were studied using a Rigaku D/max-2500 X-ray diffractometer (XRD) with Cu Kα irradiation. A Hitachi UH4150 spectrometer with an integrating sphere was used to measure the transmission spectra of the Ag NF network FTEs. The sheet resistance was measured using a four-point probe test system (Guangzhou, RTS-9). For the Joule heating treatment, constant voltages were applied to the Ag NF network FTEs using a Keithley 2636A dual-channel source meter. The surface temperature of the Ag NFs was recorded using an infrared thermometer (RNO IR-160P).

Conflicts of interest

The authors declare no competing financial interest.

Acknowledgements

The work is supported by the NSFC (No. 51872043, 51732003, 61574031), the ''111 project'' (No. B13013), the Key Research Program of Frontier Science, CAS, No. QYZDB-SSW-SLH014, and the Open Research Fund of Key laboratory of UV-emitting materials and technology, No. 130028856; this work was also supported by the Project funded by the China Postdoctoral Science Foundation (2018M640273).

References

1 A. Kim, Y. Won, K. Woo, S. Jeong and J. Moon, *Adv. Funct. Mater.*, 2014, **24**, 2462–2471.
2 T. Cheng, Y. Zhang, W.-Y. Lai and W. Huang, *Adv. Mater.*, 2015, **27**, 3349–3376.
3 X. Yang, X. T. Hu, Q. X. Wang, J. Xiong, H. J. Yang, X. C. Meng, L. C. Tan, L. Chen and Y. W. Chen, *ACS Appl. Mater. Interfaces*, 2017, **9**, 26468–26475.
4 S.-W. Kim, B. W. An, E. Cho, B. G. Hyun, Y.-J. Moon, S.-K. Kim and J.-U. Park, *Nano Lett.*, 2018, **18**, 3865–3872.
5 H.-G. Im, B. W. An, J. Jin, J. Jang, Y.-G. Park, J.-U. Park and B.-S. Bae, *Nanoscale*, 2016, **8**, 3916–3922.
6 Q. Wang, X. Hu, X. Yang, G. Liu, X. Meng, Y. Xie, Y. Xiao, J. Liu, L. Tan and Y. Chen, *Org. Electron.*, 2018, **61**, 296–303.
7 A. Kumar and C. Zhou, *ACS Nano*, 2010, **4**, 11–14.
8 N. Kim, S. Kee, S. H. Lee, B. H. Lee, Y. H. Kahng, Y.-R. Jo, B.-J. Kim and K. Lee, *Adv. Mater.*, 2014, **26**, 2268–2272.
9 S. Jiang, P.-X. Hou, M.-L. Chen, B.-W. Wang, D.-M. Sun, D.-M. Tang, Q. Jin, Q.-X. Guo, D.-D. Zhang, J.-H. Du, K.-P. Tai, J. Tan, E. I. Kauppinen, C. Liu and H.-M. Cheng, *Sci. Adv.*, 2018, **4**, eaap9264.
10 S. Bae, H. Kim, Y. Lee, X. Xu, J.-S. Park, Y. Zheng, J. Balakrishnan, T. Lei, H. R. Kim, Y. I. Song, Y.-J. Kim, K. S. Kim, B. Özyilmaz, J.-H. Ahn, B. H. Hong and S. Iijima, *Nat. Nanotechnol.*, 2010, **5**, 574–578.
11 P. Lee, J. Lee, H. Lee, J. Yeo, S. Hong, K. H. Nam, D. Lee, S. S. Lee and S. H. Ko, *Adv. Mater.*, 2012, **24**, 3326–3332.
12 B. Han, K. Pei, Y. Huang, X. Zhang, Q. Rong, Q. Lin, Y. Guo, T. Sun, C. Guo, D. Carnahan, M. Giersig, Y. Wang, J. Gao, Z. Ren and K. Kempa, *Adv. Mater.*, 2014, **26**, 873–877.
13 C. F. Guo, Q. Liu, G. Wang, Y. Wang, Z. Shi, Z. Suo, C.-W. Chua and Z. Ren, *Proc. Natl. Acad. Sci. U. S. A.*, 2015, **112**, 12332–12337.
14 H. Wu, D. Kong, Z. Ruan, P.-C. Hsu, S. Wang, Z. Yu, T. J. Carney, L. Hu, S. Fan and Y. Cui, *Nat. Nanotechnol.*, 2013, **6**, 421–425.
15 J. Lee, P. Lee, H. B. Lee, S. Hong, I. Lee, J. Yeo, S. S. Lee, T.-S. Kim, D. Lee and S. H. Ko, *Adv. Funct. Mater.*, 2013, **23**, 4171–4176.
16 P. Li, J. G. Ma, H. Y. Xu, H. C. Zhu and Y. C. Liu, *Appl. Phys. Lett.*, 2017, **110**, 161901.
17 T. Sannicolo, M. Lagrange, A. Cabos, C. Celle, J.-P. Simonato and D. Bellet, *Small*, 2016, **12**, 6052–6075.
18 A. Khan, V. H. Nguyen, D. Muñoz-Rojas, S. Aghazadehchors, C. Jiménez, N. D. Nguyen and D. Bellet, *ACS Appl. Mater. Interfaces*, 2018, **10**, 19208–19217.
19 T. C. Hauger, S. M. I. Al-Rafia and J. M. Buriak, *ACS Appl. Mater. Interfaces*, 2013, **5**, 12663–12671.
20 H.-J. Lee, S. Oh, K.-Y. Cho, W.-L. Jeong, D.-S. Lee and S.-J. Park, *ACS Appl. Mater. Interfaces*, 2018, **10**, 14124–14131.
21 Y.-R. Jang, W.-H. Chung, Y.-T. Hwang, H.-J. Hwang, S.-H. Kim and H.-S. Kim, *ACS Appl. Mater. Interfaces*, 2018, **10**, 24099–24107.
22 Y. Jin, S. Hwang, H. Ha, H. Park, S.-W. Kang, S. Hyun, S. Jeon and S.-H. Jeong, *Adv. Electron. Mater.*, 2016, **2**, 1500302.
23 P. Li, J. Ma, H. Xu, X. Xue and Y. Liu, *J. Mater. Chem. C*, 2016, **4**, 3581–3591.
24 S. Duan, Z. Wang, L. Zhang, J. Liu and C. A. Li, *Adv. Mater. Technol.*, 2018, **3**, 1800020.
25 S. Soltanian, R. Rahmanian, B. Gholamkhass, N. M. Kiasari, F. Ko and P. Servati, *Adv. Energy Mater.*, 2013, **3**, 1332–1337.
26 S.-W. Kim, B. W. An, E. Cho, B. G. Hyun, Y.-J. Moon, S.-K. Kim and J.-U. Park, *Nano Lett.*, 2018, **18**, 3865–3872.
27 B. W. An, S. Heo, S. Ji, F. Bien and J.-U. Park, *Nat. Commun.*, 2018, **9**, 2458.
28 Z. Xian, B. Han, S. Li, C. Yang, S. Wu, X. Lu, X. Gao, M. Zeng, Q. Wang, P. Bai, M. J. Naughton, G. Zhou, J.-M. Liu, K. Kempa and J. Gao, *Adv. Mater. Technol.*, 2017, **2**, 1700061.
29 S. Kiruthika, R. Gupta, K. D. M. Rao, S. Chakraborty, N. Padmavathy and G. U. Kulkarni, *J. Mater. Chem. C*, 2014, **2**, 2089–2094.
30 R. Gupta, K. D. M. Rao, K. Srivastava, A. Kumar, S. Kiruthika and G. U. Kulkarni, *ACS Appl. Mater. Interfaces*, 2014, **6**, 13688–13696.
31 B. Sciacca, J. van de Groep, A. Polman and E. C. Garnett, *Adv. Mater.*, 2016, **28**, 905–909.
32 S. Huang, Y. Liu, C. F. Guo and Z. F. Ren, *Adv. Electron. Mater.*, 2016, **2**, 1500302.

33 B. W. An, E.-J. Gwak, K. Kim, Y.-C. Kim, J. Jang, J.-Y. Kim and J.-U. Park, *Nano Lett.*, 2016, **16**, 471–478.
34 S.-Y. Min, Y. Lee, S. H. Kim, C. Park and T.-W. Lee, *ACS Nano*, 2017, **11**, 3681–3689.
35 R. Yoshikawa, M. Tenjimbayashi, T. Matsubayashi, K. Manabe, L. Magagnin, Y. Monnai and S. Shiratori, *ACS Appl. Nano Mater.*, 2018, **1**, 860–868.
36 R. Song, X. Li, F. Gu, L. Fei, Q. Ma and Y. Chai, *RSC Adv.*, 2016, **6**, 91641–91648.
37 G. H. Kim, J. H. Shin, T. An and G. Lim, *Sci. Rep.*, 2018, **8**, 13581.
38 P. C. Hsu, D. Kong, S. Wang, H. Wang, A. J. Welch, H. Wu and Y. Cui, *J. Am. Chem. Soc.*, 2014, **136**, 10593–10596.
39 A. Testa, R. Bernasconi, R. Yoshikawa, I. Takenaka, L. Magagnin and S. Shiratori, *J. Electrochem. Soc.*, 2017, **164**, D765–D770.
40 P. Li, W. Zhang, J. Ma, X. Wang, H. Xu, L. Cong and Y. Liu, *Adv. Electron. Mater.*, 2018, **4**, 1800346.
41 S. Lin, X. Bai, H. Wang, H. Wang, J. Song, K. Huang, C. Wang, N. Wang, B. Li, M. Lei and H. Wu, *Adv. Mater.*, 2017, **29**, 1703238.
42 C. C. Wu, C. I. Wu, J. C. Sturm and A. Kahn, *Appl. Phys. Lett.*, 1997, **70**, 1348–1350.
43 P. Li, H. Li, J. Ma, Y. Zhou, W. Zhang, L. Cong, H. Xu and Y. Liu, *Adv. Mater. Interfaces*, 2018, **5**, 1801287.
44 K. D. M. Rao and G. U. Kulkarni, *Nanoscale*, 2014, **6**, 5645–5651.
45 T.-B. Song, Y. Chen, C.-H. Chung, Y. Yang, B. Bob, H.-S. Duan, G. Li, K.-N. Tu, Y. Huang and Y. Yang, *ACS Nano*, 2014, **8**, 2804–2811.
46 K. L. Johnson, K. Kendal and A. D. Roberts, *Proc. R. Soc. London, Ser. A*, 1971, **324**, 301.
47 K. W. Oh, S. H. Kim and E. A. Kim, *J. Appl. Polym. Sci.*, 2001, **8**, 68–694.
48 M. Schlesinger and M. Paunovic, *Modern Electroplating*, Wiley, New York, 5th edn, 2010.
49 J. Dumesic, J. A. Koutsky and T. W. Chapman, *J. Electrochem. Soc.*, 1974, **121**, 1405–1412.
50 G. Haack, *Annu. Rev. Mater. Sci.*, 1977, **7**, 73–93.
51 P. Li, J. G. Ma, H. Y. Xu, D. Lin, X. D. Xue, X. Z. Yan, P. Xia and Y. C. Liu, *J. Alloys Compd.*, 2016, **664**, 764–769.
52 R. Gupta, A. Kumar, S. Sadasivam, S. Walia, G. U. Kulkarni, T. S. Fisher and A. Marconnet, *ACS Appl. Mater. Interfaces*, 2017, **9**, 13703–13712.
53 K. N. Tu, *J. Appl. Phys.*, 2003, **94**, 5451–5473.
54 M. L. Allen, M. Aronniemi, T. Mattila, A. Alastalo, K. Ojanpera, M. Suhonen and H. Seppa, *Nanotechnology*, 2008, **19**, 175201.
55 D. E. Sanders and A. E. DePristo, *Surf. Sci.*, 1992, **260**, 116–128.
56 S. Hong, H. Lee, J. Lee, J. Kwon, S. Han, Y. D. Suh, H. Cho, J. Shin, J. Yeo and S. H. Ko, *Adv. Mater.*, 2015, **27**, 4744–4751.
57 Q. Nian, M. Saei, Y. Xu, G. Sabyasachi, B. Deng, Y. P. Chen and G. J. Cheng, *ACS Nano*, 2015, **9**, 10018–10031.
58 H. S. Jo, S. An, J.-G. Lee, H. G. Park, S. S. Al-Deyab, A. L. Yarin and S. S. Yoon, *NPG Asia Mater.*, 2017, **9**, e347.
59 J. Jang, B. G. Hyun, S. Ji, E. Cho, B. W. An, W. H. Cheong and J.-U. Park, *NPG Asia Mater.*, 2017, **9**, e432.